Desalination and Water Treatment
www.deswater.com

doi: 10.5004/dwt.2021.27776

238 (2021) 96–104
October

Surface modified of water-soluble graphitic carbon nitride nanosheets to improve the anti-fouling performance of poly(vinylidene fluoride) membranes

Huiya Wang, Keqiang Ding*

School of Environmental Engineering, Nanjing Institute of Technology, No. 1 Hongjing Avenu Jiangning Science Park, Nanjing, Jiangsu, P.R. China, CN211167, emails: dingkq@njit.edu.cn (K.Q. Ding), whyplgl@njit.edu.cn (H.Y. Wang)

Received 2 April 2021; Accepted 9 September 2021

ABSTRACT

With the development of the economy, environmental pollution is becoming more and more serious. As a new and green separation technology, membrane separation has been paid more and more attention to environmental treatment. In this study, the poly(vinylidene fluoride) (PVDF) membrane modification was performed utilizing the water-soluble graphitic carbon nitride nanosheets in order to generate photocatalytic properties under visible light irradiation. The water-soluble g-C_3N_4 nanosheets (WS-CNNS) were successfully prepared by using the KOH/NaOH melt. The characteristics of synthesized PVDF-X membranes were determined using X-ray diffraction, Fourier-transform infrared spectra, scanning electron microscopy, transmission electronic microscopy, thermogravimetric analysis, porosity and water contact angle measurements. Basing on those characteristics, it was proved that the introduction of WS-CNNS accelerated the phase inversion of the casting solution, and made the pore diameter and pore diameter of the composite membrane change. Compared with the PVDF-0, the pure water flux of PVDF-3 increased from 90.3 to 253.7 L m^{-2} h^{-1}, the average pore size decreased from 38.02 to 12.05 nm and the contact angle of PVDF-3 decreased from 87.6° to 46.3°. Moreover, the separation of bovine serum albumin and the degradation of Methylene blue on the modified membrane was further studied. This novel PVDF membrane surface modified by WS-CNNS has a strong photocatalytic property and high application potential for water treatment.

Keywords: Photocatalytic; Water-soluble; Graphitic carbon nitride; Poly(vinylidene fluoride); Water treatment

1. Introduction

The demand for secure drinking water is increasing with the continuous growth of the population. As a new and green separation technology, membrane separation has been paid more and more attention in the field of water treatment. However, the water flux attenuation and membrane surface pollution greatly limited the practical application. It is therefore imperative to improving the anti-fouling property of the membrane [1–8].

A number of nanoparticles with photocatalytic self-cleaning performance have been studied. These studies primarily utilize the special photocatalytic performance of nanoparticles, such as the TiO_2, ZnO_2, Fe_2O_3 and $ZnIn_2S_4$. However, such oxides or sulfides of transition metals suffer from the high price and the complicated synthesis process, which greatly limits its practical application [9–12]. In recent years, graphitic carbon nitride (g-C_3N_4) has drawn attention worldwide because of its abundance, nontoxicity,

* Corresponding author.

stability and narrow bandgap, especially visible light response [13–17]. Kolesnyk et al. [18] performed poly (vinylidene fluoride) (PVDF) membrane modification utilizing g-C_3N_4 in order to generate photocatalytic properties under visible light irradiation. Compared to the pristine membrane, activation of the membrane surface with a carbonate buffer and modification with g-C_3N_4 significantly improved the membrane permeability and decreased the membrane resistance owing to changes in its hydrophilicity. Cui et al. [19] fabricated Z-scheme 2D/3D g-C_3N_4/BiOI heterojunction blended in β-phase polyvinylidene fluoride membrane (β-phase PVDF) via solvent crystallization and phase inversion technique. As expected, the designed g-C_3N_4/BiOI/β-phase PVDF photocatalytic membranes (CN/BI/β-phase PVDF PMs) achieved exceptional photocatalytic degradation efficiency for tetracycline (94.6%) as compared to the CN/BI heterojunction power (84.0%) and two other control membrane matrixes (CN/BI/PAN and CN/BI/CA PMs) within 120 min. The membrane matrix was supplemented with nano-ZnO of different content for membrane modification [19]. However, graphitic carbon nitrides tend to agglomerate because of their small size effect, which results in decreases in the reaction rate and efficiency [20–22]. It is noteworthy highlighting that few studies reported utilizing the water-soluble g-C_3N_4 nanosheets (WS-CNNS) to modify PVDF for further improving the hydrophilicity and photocatalytic activity.

Herein, we synthesized the WS-CNNS by a facile and green method to modify the PVDF membrane surface in an attempt to develop a novel method for improving the anti-biofouling performance. The performance of the modified membranes used for the decomposition of Methylene blue (MB) under visible light irradiation was evaluated. The mechanism of degradation MB by membranes was additionally assessed. This research was the potential to provide new insight into membrane material for wastewater treatment.

2. Experimental

2.1. Chemicals

Melamine was obtained from Tianjin Kermel Chemical Reagent Co., Ltd., (Tianjin, China). MB was received from Tianjin Bei Chen Fang Zheng Reagent Factory, (Tianjin, China). Sodium hydroxide (NaOH), potassium hydroxide (KOH), polyethylene glycol (PEG)6000 and bovine serum albumin (BSA) were purchased from Sinopharm Chemical Reagent Co., Ltd., (China). Sodium sulfate (Na_2SO_4) was purchased from Energy Chemical. Polyvinylidene fluoride was obtained from Shanghai Sanai Fu New Material Co., Ltd., (Shanghai, China). N,N-Dimethylformamide (DMF) was received from Sinopharm Chemical Reagent Co., Ltd., (China). All chemicals were analytical grade and used without further purification.

2.2. Synthesis of WS-CNNS

A mixture of KOH, NaOH and melamine was heated in a covered crucible at a rate of 5.0°C/min up to 360°C and maintained at that temperature for 2.0 h. The obtained solid was collected by centrifugation, washed with in 1.0 M Na_2SO_4 aqueous solution until neutral, and dried in the oven at 60°C overnight.

2.3. Membrane preparation

Firstly, 0.9 g PEG6000 was dissolved in 30 mL DMF. Then added 4.0 g PVDF slowly and raised the temperature to 60°C, and stirred for 4 h until completely dissolved. WS-CNNS was dissolved in 30 mL deionized water and then added into DMF containing PVDF drop by drop. After that, the mixture was ultrasonicated for 30 min. Then continued stirring for 2 h to obtain the evenly mixed WS-CNNS/PVDF casting solution. After standing at room temperature for 12 h, the prepared casting solution was poured on the flat membrane equipment at 25°C and scraped to form a homogeneous membrane with an average thickness of 0.2 mm. After standing in the air for about 30 s, it was immersed in the coagulation bath (deionized water) at room temperature to form a membrane and soaked in deionized water for 24 h for standby. On the basis of literature review and existing research, the WS-CNNS/PVDF composite membrane prepared in this paper was named PVDF-1, PVDF-2, PVDF-3 and PVDF-4 with the addition of WS-CNNS of 1%, 3%, 5% and 7%, respectively. The pure PVDF membrane was named PVDF-0 by the same method.

2.4. Characterizations

The properties and crystal structures of the synthesized products were characterized by the X-ray diffraction technique (XRD, Bruker D8, Germany). The morphology of the materials was inspected by scanning electron microscopy (SEM, Quanta 250 FEG). Fourier-transform infrared spectra (FT-IR, Tensor 27, USA) were recorded from 4,000 to 1,000 cm^{-1}. Thermogravimetric analysis (TGA) was performed in SDT Q600 (USA). The morphologies of WS-CNNS and the membranes were obtained with transmission electronic microscopy (TEM, FEI Tecnai G2 F20, USA). The contact angle tests were carried out by a contact angle goniometer (JY-82C, China). The phase separation rate of the casting solution was determined by the UV-Vis spectrophotometer (UV-2100, China).

2.5. Membrane performance evaluation

2.5.1. Porosity measurement

The porosity was measured by the dry wet weight method. The moisture on the surface of the wet film (5 cm × 5 cm) was dried with filter paper and weighed as W_w. Then the sample was put into a vacuum oven (60°C) for 24 h and weighed as W_d. It is calculated by Eq. (1):

$$\varepsilon = \frac{W_w - W_d}{\rho_{wA}\,\&_0} \times 100\% \tag{1}$$

where ε is the porosity of the separation membrane; W_w and W_d are the weight (g) of the membrane in the wet state and dry state respectively; A and $\&_0$ represent the area (cm^2) and thickness (cm) of the separation membrane, respectively; ρ_w is the density of pure water (g cm^{-3}).

2.5.2. Pore size determination

The average pore size of the membrane was determined by the ultrafiltration method and calculated by Eq. (2) of the Kaute–Erfurtfery equation.

$$r_m = \sqrt{\frac{(2.9 - 1.75\varepsilon) \times 8\eta l Q}{\varepsilon \times A \times \Delta P}} \quad (2)$$

where η is the viscosity of water (8.9 × 10^{-4} Pa·s); ε is the porosity (%), l is the thickness of the membrane (2 × 10^{-4} m); Q is the water flux per unit time (m^3 s^{-1}); A is the effective area of the membrane (m^2), and ΔP is the device pressure (0.1 MPa).

2.5.3. Flux measurement of PVDF-X composite membrane

The self-made ultrafiltration device (500 mL) was used to test the filtration performance (shown as Fig. 1), including the pure water flux, the BSA rejection rate and the recovery rate. The original concentration of BSA was 1 g L^{-1}, the test conditions were room temperature, 0.1 MPa operating pressure, and the effective area of the separation membrane a = 50 cm^{-2}. The specific test process is as follows:

- Put the separation membrane into the filter device and added 200 mL pure water. Press the membrane at 0.15 MPa for 30 min under N_2. Adjusted the pressure to 0.1 MPa after stabilization and collected data after the stable flux of water.
- The pure water flux (J_w/L m^{-2} h^{-1}) can be calculated by Eq. (3) when the test pressure was 0.1 MPa and the volume of pure water filtered through the membrane was v.
- After filtering pure water for a certain time (30–60 min), changed the pure water in the ultrafiltration cup into BSA solution (C_f = 1 g L^{-1}) and collected the filtration volume (V) of the ultrafiltration membrane within a certain time (t) under the same test pressure of 0.1 MPa, which can be calculated by Eq. (3). At the same time, a UV-2100 spectrophotometer was used to measure the absorbance of the initial and filter solution at 280 nm, and the BSA concentration C_p in the filtration night was converted. Combined with the initial concentration C_f, the BSA rejection rate R of the separation membrane could be calculated by Eq. (4).
- After filtration of BSA solution for 30 min, the membrane was taken out and washed repeatedly with deionized water for 5 min, and then step (2) was repeated to obtain the pure water flux J_r after washing.
- Each filtration of pure water BSA solution is a cycle, and each membrane is tested for three cycles, followed by 120 min pure water flux test water flux cycle test to verify its pollution resistance, and the corresponding J_w, J_P, J_R and R after each test are recorded.

The pure water flux and BSA protein rejection were calculated according to the following equations:

$$J_w = \frac{V_w}{A \times t} \quad (3)$$

$$\frac{V_p}{A \times t} R = \left(1 - \frac{C_p}{C_f}\right) \times 100\% \quad (4)$$

where J_w is the pure water flux (L m^{-2} h^{-1}); V_w (L) is the volume of pure water passing through the membrane; V_p (L) is the volume passing through the bovine serum albumin solution. t is filtrate volume (L) and filtration time (h), respectively; A is the effective area of separation membrane (m^2); R is the rejection rate (%) of BSA; C_p and C_f were BSA concentration (g L^{-1}) of filter solution and the stock solution respectively.

2.5.4. Membrane antifouling experiments

The antifouling performance of the separation membrane can be evaluated by the recovery rate of water flux (FRR). The higher the recovery rate of water flux, the better the antifouling performance of the surface membrane. FRR can be calculated by Eq. (5):

$$\mathrm{FRR} = \frac{J_r}{J_w} \times 100\% \quad (5)$$

The antipollution performance of the separation membrane can also be evaluated by the total pollution rate (R_t, %). The total pollution rate includes reversible pollution rate (R_r, %) and irreversible pollution rate (R_{ir}, %). The specific calculation formula is as follows:

$$R_t = \frac{J_w - J_p}{J_w} \times 100\% \quad (6)$$

$$R_r = \frac{J_r - J_p}{J_w} \times 100\% \quad (7)$$

$$R_{ir} = \frac{J_w - J_r}{J_w} \times 100\% \quad (8)$$

2.5.5. Photocatalytic activity tests

The photocatalytic degradation experiments were tested by degradation of MB (10 ppm) using a 500 W Xenon lamp acting as a light source. In a typical experiment, PVDF-3 (5 cm × 5 cm) and 100 mL MB solution were put in a quartz tube reactor and thoroughly stirred uniformly to form a suspension. Then the mixture solution was stirring for 60 min in the dark to reach the adsorption–desorption equilibrium before turning on the xenon lamp. After turning on the light, 1 mL of suspension was collected at certain time intervals and the photocatalysts were separated by filtration with 0.22 mm. The concentration of MB was detected by UV-2100.

3. Results and discussion

3.1. Characterization of WS-CNNS and the modified membranes

From the SEM and TEM results in Fig. 2, it can be seen that the WS-CNNS appears as a 2D sheet-like

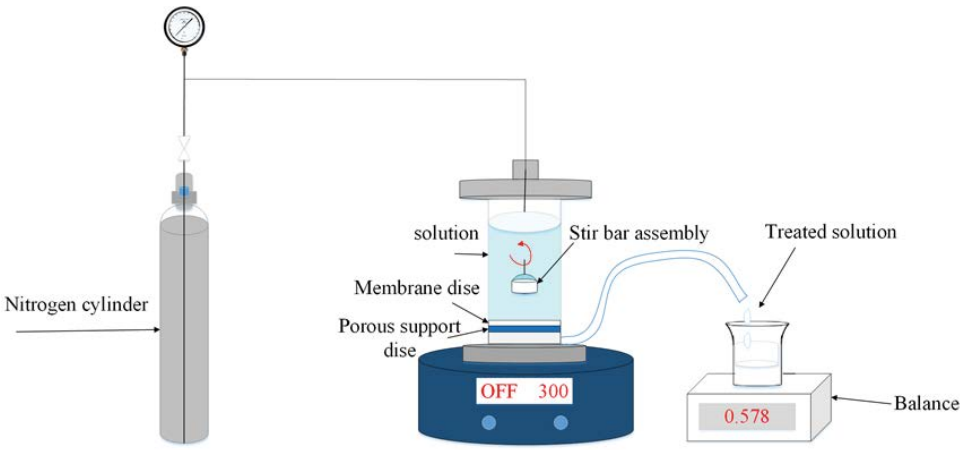

Fig. 1. Ultrafiltration device.

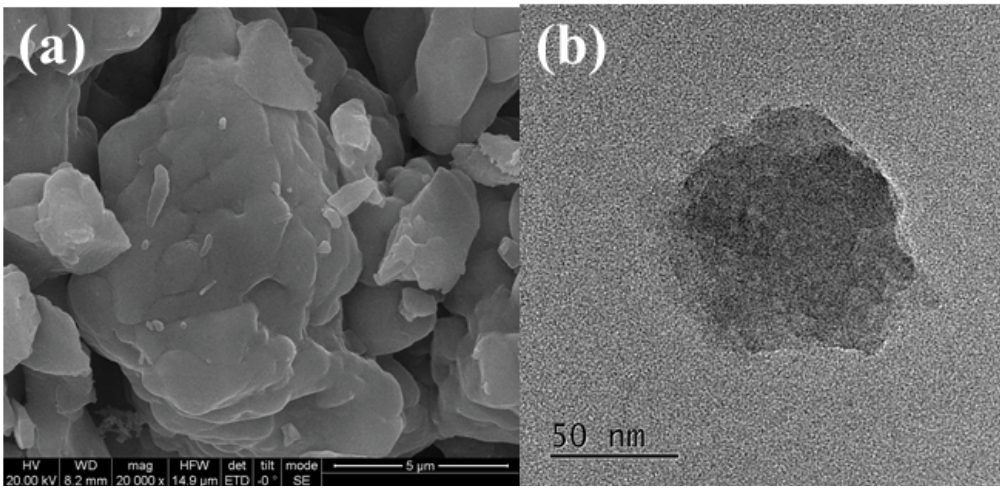

Fig. 2. (a) Scanning electron microscopy and (b) transmission electronic microscopy pictures of water-soluble g-C_3N_4 nanosheets.

structure, which was the same as the structure reported by Igor et al. [23] and indicated that, we successfully synthesized WS-CNNS. FT-IR spectroscopy was conducted to investigate the chemical structure of WS-CNNS, and the results are shown in Fig. 3. The peak at 3,450 cm^{-1} may be assigned to the stretching vibrations of OH^- groups incorporated into the poly(heptazine imide) structure as a result of the alkali melt treatment. The peaks that appeared in the range 2,150–2,175 cm^{-1} may be assigned to the υ(C≡N) vibrations [24].

XRD patterns were used to analyze the crystallization of the PVDF-X composite membrane. As shown in Fig. 4a, the pure PVDF-0 showed a diffraction peak at 2θ = 19.7° corresponding to the diffraction peak of the α-phase. Notably, the diffraction peak of the α-phase-shifted to 20.7 after coating with WS-CNNS, indicating there is an interaction between WS-CNNS and PVDF [24–26]. To characterize the chemical structure of the PVDF-X composite membrane, FT-IR experiments were also conducted and results are shown in Fig. 4b. The absorption bands were observed at 763 and 976 cm^{-1} corresponding to typical vibration characteristics of the nonpolar α-phase. After coating with WS-CNNS,

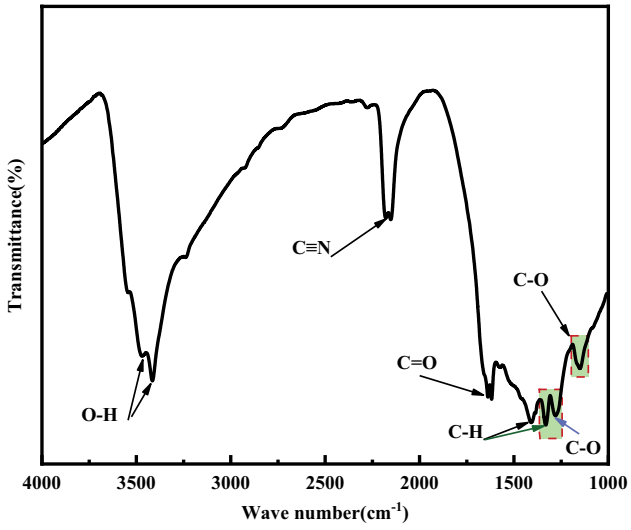

Fig. 3. Fourier-transform infrared spectra of water-soluble g-C_3N_4 nanosheets.

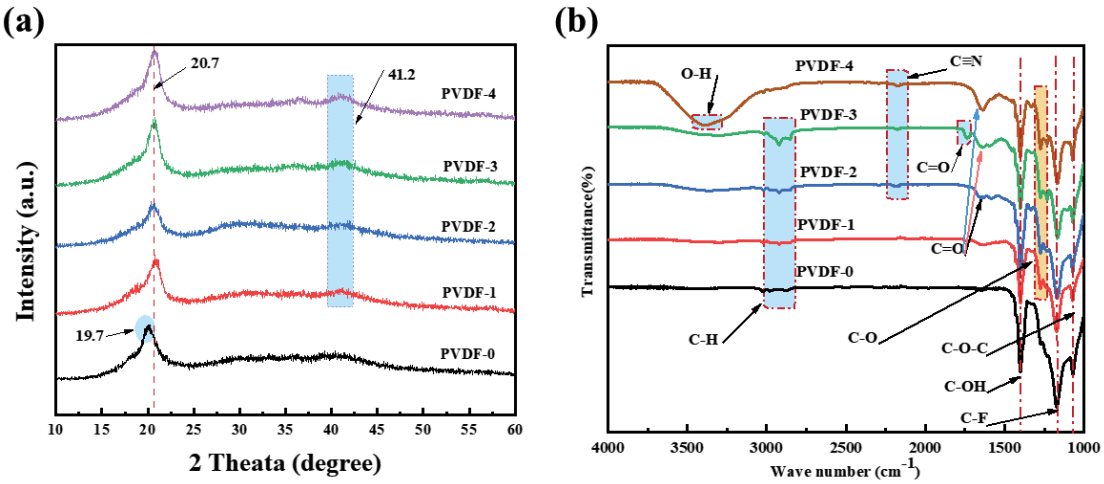

Fig. 4. (a) X-ray diffraction pattern and (b) Fourier-transform infrared spectra of PVDF-0 and PVDF-X.

the intensity of WS-CNNS absorption bands increased gradually with an increase in the WS-CNNS content. Notably, the hydrophilic groups (such as –OH) in WS-CNNS greatly increase hydrophilicity, which can effectively restrain the foulant adhesion and improve the antifouling tendency [27].

The morphologies of the obtained membranes were examined by SEM. Fig. 5a reveals that the upper surface of pure PVDF-0 was smooth without obvious holes. At 5,000 times magnification, the scanning images showed that PVDF-0 was loose and open according to SEM at the bottom of the membrane. Notably, the pores at the bottom of the membrane were uniform and dense after the addition of WS-CNNS (Fig. 5b–e). WS-CNNS appeared in PVDF-X and adhered to each other. The bottom of PVDF-4 was the densest, but almost no microspheres were observed. The reasons for these differences were as follows: (1) when hydrophobic PVDF and hydrophilic WS-CNNS were mixed, which produced strong repulsive force, led to the existence of large interfacial pressure between them and was conducive to the formation of interfacial pores in the process of phase separation. (2) The addition of WS-CNNS accelerated the solvent nonsolvent diffusion, which was conducive to the formation of porous structure and microspheres, which is consistent with the change of phase separation rate. The cross-section of the PVDF-X was the typical asymmetric structure. This was due to the outer surface of the membrane being first contacted with air and then immerses in water for phase transformation [28,29]. The solvent on the surface of the casting solution had a volatilization process and the solvent was directly exchanged with water, resulting in the formation of an asymmetric structure. With the addition of WS-CNNS, the finger-like pores in the cross-section of the PVDF-3 membrane first increased and then disappeared. The finger-like pores in the PVDF-3 membrane were the widest and most orderly, and the channels were smoother and connected up and down. The change of membrane cross-section shape was largely

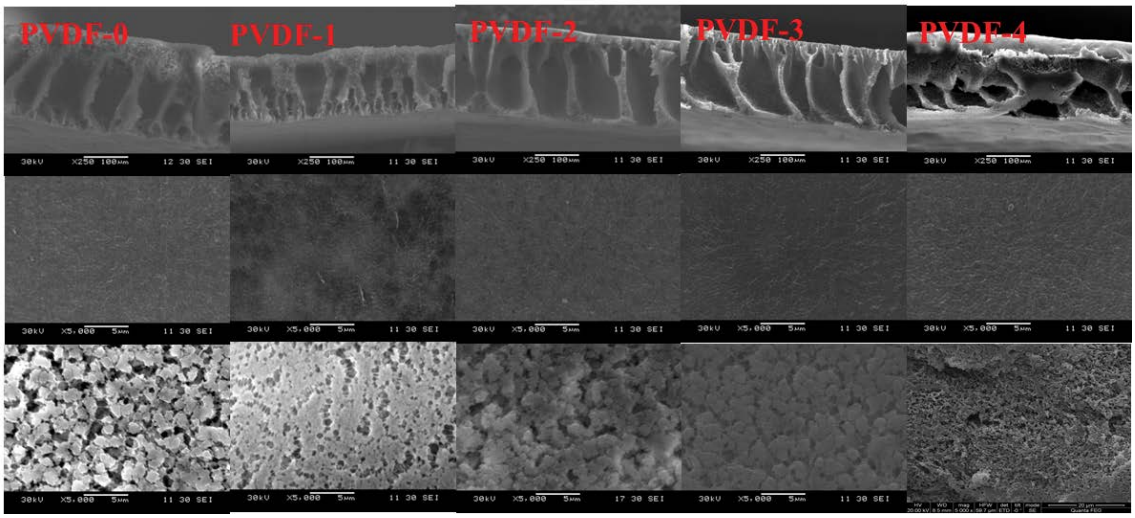

Fig. 5. Scanning electron microscopy morphologies of (a) PVDF-0, (b) PVDF-1, (c) PVDF-2, (d) PVDF-3 and (e) PVDF-4.

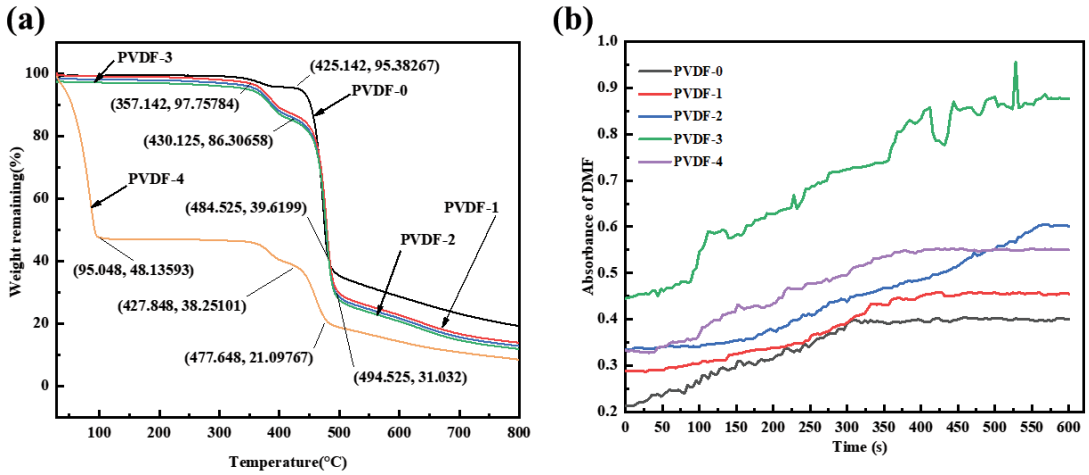

Fig. 6. (a) Thermogravimetric analysis and (b) split-phase velocity of PVDF-0 and PVDF-X.

determined by thermodynamics and kinetics involved in phase transformation, polymer-solvent interaction and solvent nonsolvent exchange rate [30]. No WS-CNNS aggregation was found at the bottom of the membrane or at the top surface of the membrane, indicating that WS-CNNS were uniformly dispersed in the PVDF matrix.

The pyrolysis process of the PVDF membrane changed obviously after adding WS-CNNS and the TGA analysis results of PVDF-0 and PVDF-X are compared in Fig. 6a. Clearly, the decomposition temperature of the PVDF-0 was at about 425°C, which was higher than PVDF-X. Moreover, with the increase of WS-CNNS content, the pyrolysis temperature decreased gradually, which can be attributed to the decomposition of WS-CNNS in PVDF-X. This phenomenon showed that the added WS-CNNS affected the grain size and the void size of the PVDF formed in the process of membrane formation [31,32].

The split-phase velocity of PVDF-0 and PVDF-X are shown in Fig. 6b. Clearly, the phase separation rate first increased and then decreased with the increase of WS-CNNS content. This phenomenon was closely related to the content of WS-CNNS and the viscosity of the casting solution. In general, the addition of hydrophilic materials would accelerate the exchange of solvent and non-solvent in the process of phase transformation. On the other hand, with the increase of WS-CNNS content, the increase of viscosity of casting solution would lead to the decrease of phase separation rate of the casting solution. When the content of WS-CNNS was low, the hydrophilicity of the PVDF membrane would greatly influence the phase separation rate and increased the phase separation rate. When the content of WS-CNNS reached a certain level, the viscosity would be too high, which would affect the phase separation process and decreased the phase separation rate [33].

3.2. Membrane performance

As shown in Table 1, the ultrafiltration performance of PVDF-3 was the best. Compared with the PVDF-0, the pure water flux of PVDF-3 increased from 90.3 to 253.7 L m^{-2} h^{-1}, the average pore size decreased from 38.02 to 12.05 nm and the contact angle of PVDF-3 decreased from 87.6° to 46.3°. These results have shown that the hydrophilicity of the PVDF membrane increased slightly after coating with WS-CNNS. On the other hand, coating with WS-CNNS changed the pores and increased the number of pores, which was helpful to improve the water flux. Moreover, BSA rejection of modified PVDF membrane containing various concentrations of WS-CNNS is further illustrated in Table 1. Clearly, the BSA rejection was increased by loading WS-CNNS into the PVDF membrane. This behavior could be attributed to the reduction of pore size of PVDF-X membrane compared with pure PVDF membranes [34,35].

The stronger the anti-fouling performance, the higher the flux recovery. As shown in Fig. 7a, the flux recovery rates of PVDF-X membrane were superior to PVDF-0 and the total pollution rates R_t were lower than PVDF-0. Moreover, the corresponding reversible pollution and irreversible pollution were also reduced compared with PVDF-0. These phenomena may be due to the hydrophilicity of the membrane. The hydrophilicity of PVDF-0 was increased after coating with WS-CNNS, which was easier to form a hydration layer and reduce the contact between the membrane and the pollutant [36–38]. The introduction of WS-CNNS would greatly enhance the anti-fouling property of the PVDF-0. To further investigate the anti-fouling of PVDF-X membranes, a repeated experiment with five cycles was performed. As displayed in Fig. 7b, all the PVDF-X membranes retained the superior pure water flux performance after five recycles experiments, indicating excellent reusability.

3.3. Photocatalytic experiments

MB was chosen as representatives of organic pollutants to evaluate the photocatalytic activity of membranes modified with WS-CNNS. At the first stage, adsorption of MB by PVDF-3 membrane from the solutions of an initial concentration of 10 ppm before turning on the xenon lamp was conducted to reach the adsorption-desorption equilibrium [39]. After turning on the light, it can be seen from

Table 1
Performance of the PVDF-0 and PVDF-X membranes

Membrane	ε	r_m	J_w	J_P	R	Contact angle
	(%)	(nm)	(L m^{-2} h^{-1})	(L m^{-2} h^{-1})	(%)	(°)
PVDF-0	50.60	38.02	90.3	35.6	48.4	87.6
PVDF-1	76.60	23.93	110.8	98.64	77.8	67.9
PVDF-2	81.60	30.07	176	137.6	84.7	66.0
PVDF-3	86.98	12.05	253.7	208.6	94.4	46.3
PVDF-4	84.57	11.405	217.6	174.08	95.8	59.3

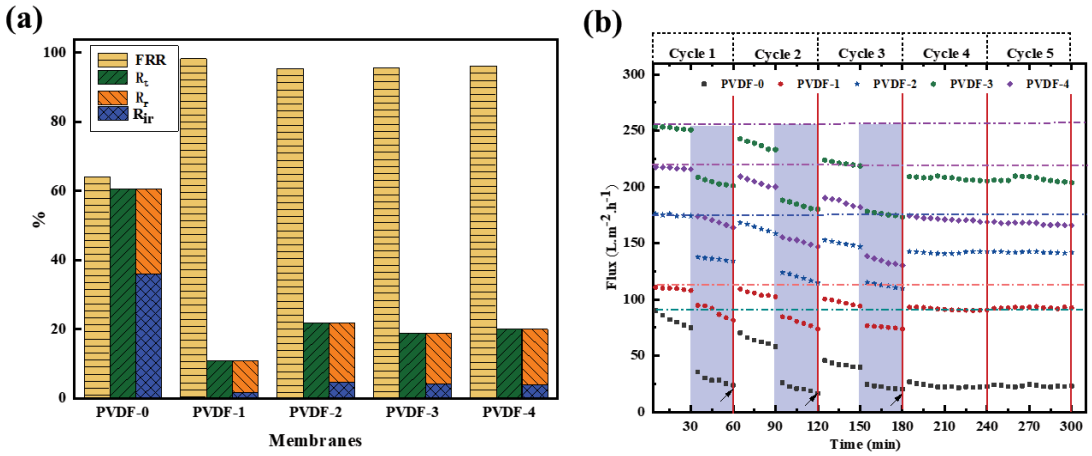

Fig. 7. (a) Comparison of the FRR, R_t, R_r, and R_{ir} of PVDF-0 and PVDF-X membranes. (b) Cycling runs for the anti-fouling over PVDF-0 and PVDF-X membranes.

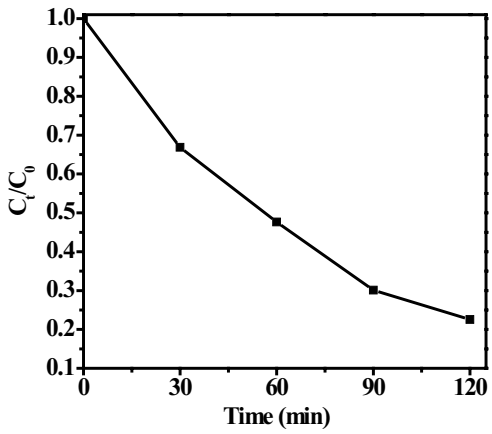

Fig. 8. Methylene blue degradation for the photocatalytic degradation of Methylene blue by PVDF-3.

Fig. 8 that the degradation of Methylene blue was obvious, indicating that PVDF-3 had excellent photocatalytic activity [40–43].

4. Conclusions

The PVDF membranes modified with WS-CNNS were investigated for BSA separation and MB degradation. The SEM images of membranes indicated that the distribution of WS-CNNS into the PVDF and the WS-CNNS had an important role in the performance of synthesized PVDF-X membranes. It has been proved that the introduction of WS-CNNS accelerated the phase inversion of the casting solution, and made the pore diameter and pore diameter of the composite membrane change. Moreover, the pure water flux of PVDF-3 increased from 90.3 to 253.7 L m^{-2} h^{-1}, the average pore size decreased from 38.02 to 12.05 nm and the contact angle of PVDF-3 decreased from 87.6° to 46.3° compared with the PVDF-0. The incorporation of WS-CNNS increased the hydrophilicity of PVDF, which improved the performance of the membrane toward the separation of BSA and the degradation of MB. This study is expected to provide a new perspective for the development of efficient and stable membranes and has a potential application prospect.

Acknowledgments

Thanks to Jiangsu Province's scientific and technological achievements in a special fund project (BA2018004) for the support of this work.

References

[1] X.-T. Yuan, H.-Z. Geng, L. Wu, L. Wang, W.Y. Wang, X.-S. Yuan, B.Q. He, Y.-X. Jiang, Y.-J. Ning, Z.-R. Zhu, J.X. Li, Polyaniline/

polysulfone ultrafiltration membranes with improved permeability and anti-fouling behavior, J. Water Process Eng., 40 (2014) 101903, doi: 10.1016/j.jwpe.2020.101903.
[2] S. Xiang, J.K. Yang, Z.Y. Cui, S.H. Qin, Q.Q. Qin, Preparation of hollow fiber membrane via grafting tannic acid and its influence on microstructure, permeability and anti-fouling, ACS Mater. Lett., 285 (2021) 129095, doi: 10.1016/j.matlet.2020.129095.
[3] A. Ahmad Khan, M. Irfan Siyal, J.-O. Kim, Fluorinated silica–modified anti–oil-fouling omniphobic F–SiO_2@PES robust membrane for multiple foulants feed in membrane distillation, Chemosphere, 263 (2021) 128140, doi: 10.1016/j.chemosphere.2020.128140.
[4] C. Liu, W.J. Wang, B. Yang, K. Xiao, H.Z. Zhao, Separation, anti-fouling, and chlorine resistance of the polyamide reverse osmosis membrane: from mechanisms to mitigation strategies, Water Res., 195 (2021) 116976, doi: 10.1016/j.watres.2021.116976.
[5] D. Rana, K. Bag, S.N. Bhattacharyya, B.M. Mandal, Miscibility of poly(styrene-*co*-butyl acrylate) with poly(ethyl methacrylate): existence of both UCST and LCST, J. Polym. Sci. Polym. Phys., 38 (2000) 369–375.
[6] D. Rana, B.M. Mandal, S.N. Bhattacharyya, Analogue calorimetric studies of blends of poly(vinyl ester)s and polyacrylates, Macromolecules, 29 (1996) 1579–1583.
[7] D. Rana, B.M. Mandal, S.N. Bhattacharyya, Analogue calorimetry of polymer blends: poly(styrene-*co*-acrylonitrile) and poly(phenyl acrylate) or poly(vinyl benzoate), Polymer, 37 (1996) 2439–2443.
[8] D. Rana, B.M. Mandal, S.N. Bhattacharyya, Miscibility and phase diagrams of poly(phenyl acrylate) and poly(styrene-*co*-acrylonitrile) blends, Polymer, 34 (1993) 1454–1459.
[9] J.-P. Méricq, J. Mendret, S. Brosillon, C. Faur, High performance PVDF-TiO_2 membranes for water treatment, Chem. Eng. Sci., 123 (2015) 283–291.
[10] J.M. Hong, Y. He, Polyvinylidene fluoride ultrafiltration membrane blended with nano-ZnO particle for photo-catalysis self-cleaning, Desalination, 332 (2014) 67–75.
[11] A. Alpatova, M. Meshref, K.N. McPhedran, M.G. El-Din, Composite polyvinylidene fluoride (PVDF) membrane impregnated with Fe_2O_3 nanoparticles and multiwalled carbon nanotubes for catalytic degradation of organic contaminants, J. Membr. Sci., 490 (2015) 227–235.
[12] T.T. Liu, L. Wang, X. Liu, C.X. Sun, Y.T. Lv, R. Miao, X.D. Wang, Dynamic photocatalytic membrane coated with $ZnIn_2S_4$ for enhanced photocatalytic performance and antifouling property, Chem. Eng. J., 379 (2019) 122379, doi: 10.1016/j.cej.2019.122379.
[13] Y.L. Yang, B.D. Mao, G. Gong, D. Li, Y.H. Liu, W.J. Cao, L. Xing, J. Zeng, W.D. Shi, S.Q. Yuan, In-situ growth of Zn–$AgIn_5S_8$ quantum dots on g-C_3N_4 towards 0D/2D heterostructured photocatalysts with enhanced hydrogen production, Int. J. Energy Res., 44 (2019) 15882–15891.
[14] L. Wang, H.-g. Zhang, C.-y. Guo, L.-j. Feng, C.-h. Li, W.-t. Wang, Facile constructing plasmonic Z-scheme Au NPs/g-C_3N_4/BiOBr for enhanced visible light photocatalytic activity, J. Fuel Chem. Technol., 47 (2019) 834–842.
[15] S. Jasminder, K. Pooja, B. Soumen, Degradation of toxic industrial dyes using SnO_2/g-C_3N_4 nanocomposites: role of mass ratio on photocatalytic activity, J. Photochem. Photobiol., A, 371 (2019) 136–143.
[16] S.H. Cao, Y. Zhang, N.N. He, J. Wang, H. Chen, F. Jiang, Metal-free 2D/2D heterojunction of covalent triazine-based frameworks/graphitic carbon nitride with enhanced interfacial charge separation for highly efficient photocatalytic elimination of antibiotic pollutants, J. Hazard. Mater., 391 (2020) 122204, doi: 10.1016/j.jhazmat.2020.122204.
[17] W.L. Xue, S.H. Cao, R. Liu, R. Tang, H. Chen, F. Jiang, Preparation of nitrogen-containing carbon using a one-step thermal polymerization method for activation of peroxymonosulfate to degrade bisphenol A, Chemosphere, 248 (2020) 126053, doi: 10.1016/j.chemosphere.2020.126053.
[18] I. Kolesnyk, J. Kujawa, H. Bubela, V. Konovalova, A. Burban, A. Cyganiuk, W. Kujawski, Photocatalytic properties of PVDF membranes modified with g-C_3N_4 in the process of Rhodamines decomposition, Sep. Purif. Technol., 250 (2020) 117231, doi: 10.1016/j.seppur.2020.117231.
[19] Y.H. Cui, L.L. Yang, J. Zheng, Z.K. Wang, B.R. Li, Y. Yan, M.J. Meng, Synergistic interaction of Z-scheme 2D/3D g-C_3N_4/BiOI heterojunction and porous PVDF membrane for greatly improving the photodegradation efficiency of tetracycline, J. Colloid Interface Sci., 586 (2021) 335–348.
[20] Y. Li, X.Y. Xing, J.Z. Pei, R. Li, Y. Wen, S.C. Cui, T. Liu, Automobile exhaust gas purification material based on physical adsorption of tourmaline powder and visible light catalytic decomposition of g-C_3N_4/$BiVO_4$, Ceram. Int., 46 (2020) 12637–12647.
[21] H. Zhang, L.H. Jia, P. Wu, R.J. Xu, J. He, W. Jiang, Improved H_2O_2 photogeneration by KOH-doped g-C_3N_4 under visible light irradiation due to synergistic effect of N defects and K modification, Appl. Surf. Sci., 527 (2020) 146584, doi: 10.1016/j.apsusc.2020.146584.
[22] L.F. Pan, S.H. Cao, R. Liu, H. Chen, F. Jiang, X. Wang, Graphitic carbon nitride grown in situ on aldehyde-functionalized α-Fe_2O_3: all-solid-state Z-scheme heterojunction for remarkable improvement of photo-oxidation activity, J. Colloid Interface Sci., 548 (2019) 284–293.
[23] K. Igor, M. Dariusz, A. Christiane, I. Marina, S. Mariana, M. Luís, N. Christof, T. Andrey, C.Y. Li, D. Benjamin, L. Robert, B. Johannes, K. Ute, C.B. Im, K. Björn, J. Timo, B. Radim, Water-soluble polymeric carbon nitride colloidal nanoparticles for highly selective quasi-homogeneous photocatalysis, Angew. Chem. Int. Ed., 559 (2020) 487–495.
[24] M.V. Arularasu, M. Harb, R. Vignesh, T.V. Rajendran, R. Sundaram, PVDF/ZnO hybrid nanocomposite applied as a resistive humidity sensor, Surf. Interfaces, 21 (2020) 100780, doi: 10.1016/j.surfin.2020.100780.
[25] W. Ma, B.H. Yao, W. Zhang, Y.Q. He, Y. Yu, J.F. Niu, Fabrication of PVDF-based piezocatalytic active membrane with enhanced oxytetracycline degradation efficiency through embedding few-layer E-MoS_2 nanosheets, Chem. Eng. J., 415 (2021) 129000, doi: 10.1016/j.cej.2021.129000.
[26] A.K. Tripathi, R. Sekar, P.K.C. Pillai, XRD studies of a $BaTiO_3$: PVDF composite, ACS Mater. Lett., 9 (1989) 24–28.
[27] W.J. Xie, L.Q. Tian, K.F. Wu, B.D. Guo, J.R. Gong, Understanding and modulating exciton dynamics of organic and low-dimensional inorganic materials in photo(electro)catalysis, J. Catal., 396 (2021) 91–104.
[28] D.L. Li, X.H. Sun, C.L. Gao, M.D. Dong, Improved water flux and antifouling properties of cardo poly(aryl ether ketone) ultrafiltration membrane by novel sulfobetaine polyimides additive, Sep. Purif. Technol., 251 (2020) 117144, doi: 10.1016/j.seppur.2020.117144.
[29] W.J. Lee, Y.P. Bao, C.T. Guan, X. Hu, T.-T. Lim, Ce/TiO_x-functionalized catalytic ceramic membrane for hybrid catalytic ozonation-membrane filtration process: fabrication, characterization and performance evaluation, Chem. Eng. J., 410 (2021) 128307, doi: 10.1016/j.cej.2020.128307.
[30] P. van de Witte, P.J. Dijkstra, J.W.A. van den Berg, J. Feijen, Phase separation processes in polymer solutions in relation to membrane formation, J. Membr. Sci., 117 (1996) 1–31.
[31] H.B. Li, W.Y. Shi, Y.F. Zhang, R. Zhou, H.X. Zhang, Preparation of hydrophilic PVDF/PPTA blend membranes by in situ polycondensation and its application in the treatment of landfill leachate, Appl. Surf. Sci., 346 (2015) 134–146.
[32] J. Schnittger, J. McCutcheon, T. Hoyer, M. Weyd, G. Fischer, P. Puhlfürß, M. Halisch, I. Voigt, A. Lerch, Hydrophobic ceramic membranes in MD processes – impact of material selection and layer characteristics, J. Membr. Sci., 618 (2021) 118678, doi: 10.1016/j.memsci.2020.118678.
[33] D. Zhang, S.F. Li, Y. Li, Pore-scale investigation on the effect of gas-liquid phase separation on reactive flow in a horizontal rough fracture using the lattice Boltzmann method, Chem. Eng. Sci., 236 (2021) 116483, doi: 10.1016/j.ces.2021.116483.
[34] Z.H. Guo, Y. Yang, S. Xiang, X. Du, Z.Y. Cui, B.Q. He, H. Wang, J.X. Li, T. Jiang, Preparation of PVDF membrane based on "In-situ Template-TIPS" technology and the investigation on membrane formation mechanism, microstructure regulation

and permeability, J. Membr. Sci., 620 (2021) 118839, doi: 10.1016/j.memsci.2020.118839.
[35] A. Ilyas, M. Mertens, S. Oyaert, I.F.J. Vankelecom, Anti-fouling behavior of micro-patterned PVDF membranes prepared via spray-assisted phase inversion: influence of pattern shapes and flow configuration, Sep. Purif. Technol., 259 (2021) 118041, doi: 10.1016/j.seppur.2020.118041.
[36] M. He, L. Wang, Y.T. Lv, X.D. Wang, Z. Zhang, Q. Cui, J. Zhu, Effect of a novel hydrophilic double-skinned support layer on improving anti-fouling performance of thin-film composite forward osmosis membrane, Colloids Surf., A, 602 (2020) 125081, doi: 10.1016/j.colsurfa.2020.125081.
[37] J.H. Zhang, N. Li, D. Wang, J.M. Li, Y. Chen, Z. Wang, Omniphobic palygorskite coated Janus membrane with enhanced fouling and wetting resistance for direct contact membrane distillation, Desalination, 505 (2021) 114986, doi: 10.1016/j.desal.2021.114986.
[38] L. Zhang, R. Takagi, S.Y. Wang, Y.Q. Lin, K.C. Guan, L. Cheng, H. Matsuyama, In situ formation of ultrathin polyampholyte layer on porous polyketone membrane via a one-step dopamine co-deposition strategy for oil/water separation with ultralow fouling, J. Membr. Sci., 619 (2021) 118789, doi: 10.1016/j.memsci.2020.118789.
[39] R. Ding, S.H. Cao, H. Chen, F. Jiang, X. Wang, Preparation of tellurium doped graphitic carbon nitride and its visible-light photocatalytic performance on nitrogen fixation, Colloids Surf., A, 563 (2019) 263–270.
[40] S.H. Cao, Z.Y. Jiao, H. Chen, F. Jiang, X. Wang, Carboxylic acid-functionalized cadmium sulfide/graphitic carbon nitride composite photocatalyst with well-combined interface for sulfamethazine degradation, J. Photochem. Photobiol., A, 364 (2018) 22–31.
[41] W.Q. Cui, D.M. Guo, L. Liu, J.S. Hu, D. Rana, Y.H. Liang, Preparation of $ZnIn_2S_4/K_2La_2Ti_3O_{10}$ composites and their photocatalytic H_2 evolution from aqueous Na_2S/Na_2SO_3 under visible light irradiation, Catal. Commun., 48 (2014) 55–59.
[42] W.Q. Cui, Y.L. Qi, L. Liu, D. Rana, J.S. Hu, Y.H. Liang, Synthesis of $PbS–K_2La_2Ti_3O_{10}$ composite and its photocatalytic activity for hydrogen production, Prog. Nat. Sci., 22 (2012) 120–125.
[43] W.Q. Cui, M.Y. Shao, L. Liu, Y.H. Liang, D. Rana, Enhanced visible-light-responsive photocatalytic property of PbS-sensitized $K_4Nb_6O_{17}$ nanocomposite photocatalysts, Appl. Surf. Sci., 276 (2013) 823–831.